Supercritical Carbon Dioxide Anchored Fe_3O_4 Nanoparticles on Graphene Foam and Lithium Battery Performance

Xuebo Hu,[†] Minhao Ma,[†] Mengqi Zeng,[†] Yangyong Sun,[†] Linfeng Chen,[†] Yinghui Xue,[†] Tao Zhang,[†] Xinping Ai,[†] Rafael G. Mendes,[‡] Mark H. Rümmeli,[‡] and Lei Fu*,[†]

[†]College of Chemistry and Molecular Science, Wuhan University, Wuhan 430072, People's Republic of China
[‡]IFW Dresden, P.O. Box 270116, Dresden 01069, Germany

Ⓢ Supporting Information

ABSTRACT: Magnetite (Fe_3O_4) is an attractive electrode material due to its high theoretical capacity, eco-friendliness, and natural abundance. However, its commercial application in lithium-ion batteries is still hindered by its poor cycling stability and low rate capacity resulting from large volume expansion and low conductivity. We present a new approach which makes use of supercritical carbon dioxide to efficiently anchor Fe_3O_4 nanoparticles (NPs) on graphene foam (GF), which was obtained by chemical vapor deposition in a single step. Without the use of any surfactants, we obtain moderately spaced Fe_3O_4 NPs arrays on the surface of GF. The particle size of the Fe_3O_4 NPs exhibits a narrow distribution (11 ± 4 nm in diameter). As a result, the composites deliver a high capacity of about 1200 mAh g^{-1} up to 500 cycles at 1 C (924 mAh g^{-1}) and about 300 mAh g^{-1} at 20 C, which reaches a record high using Fe_3O_4 as anode material for lithium-ion batteries.

KEYWORDS: supercritical CO_2, lithium-ion battery, graphene foam, Fe_3O_4 nanoparticles
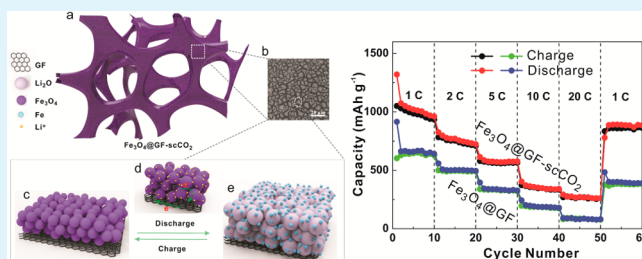
■ INTRODUCTION

Rechargeable lithium-ion batteries (LIBs) are the dominant power supplier for tablet computers and smartphones. In order to meet the growing demand for electricity guzzling portable electronic devices, the development of advanced electrodes with high capacity, excellent cycling performance and rate capability is urgently needed.[1−4] Materials that undergo a conversion reaction with lithium often involve more than one electron transfer per transition-metal cation during redox processes, and are promising candidates for high-capacity anodes materials for LIBs.[5] Among the transition metal oxides undergoing a conversion reaction with lithium, magnetite (Fe_3O_4) attracts particular attention because of its high theoretical capacity (924 mAh g^{-1}, about 3 times higher than that of graphite anodes), eco-friendliness, and natural abundance.[5−7] However, its commercial application in lithium-ion batteries is still hindered by its poor reaction kinetics (e.g., poor cycling stability and low rate capacity) resulting from large volume expansion and low conductivity.[8,9] In principle, a self-organized Fe_3O_4 nanoparticals (NPs) layer would be helpful to resolve these issues because they have a larger surface-to-volume ratio and short lithium-ion (and electron) diffusion path lengths.[10−13] Furthermore, they could easily accommodate the volume expansion−contraction that occurs during cycling.[14−17]

Recently, graphene has been shown to be a promising framework to host and disperse Fe_3O_4 NPs. Moreover, graphene can facilitate ion and electron transport and release

mechanical stress during Li-ion insertion/extraction cycling. Its superior chemical stability and increased heat transfer ability are additional factors favoring its use over commercial LIBs.[14,18−20] The small Fe_3O_4 particles dispersed in graphene with ultrahigh specific surface area also often lead to new reaction pathways with lithium, as well as the formation and stabilization of kinetically stable phases. A number of surfactants have been used to stabilize graphene oxide (GO) and Fe_3O_4 NPs (with particle sizes in the range of 100−300 nm).[21,22] Although they show improved performance (∼900−1050 mAh g^{-1} up to 100 cycles at 93 mA g^{-1}), the extra additives inevitably reduce the overall electrical conductivity of the composites.[23] Moreover, the electron and ion transport pathways are formed by random oriented oxides on reduced graphene sheets, which are poorly controlled and ineffective. Another commonly encountered challenge in using transition metal oxides (including Fe_3O_4) for LIBs electrode materials is achieving strong adhesion between the well-dispersed metal oxides NPs and the graphene hosts. Otherwise, the active materials (Fe_3O_4 NPs) will detach from the graphene due to severe volume change during Li-ion insertion/extraction cycling. This decoupling of the active material generally leads to significant capacity degradation, low rate capacity, and poor cyclability.[24] For better control, Luo et al. grafted mesoporous Fe_3O_4 nanostructures onto three-
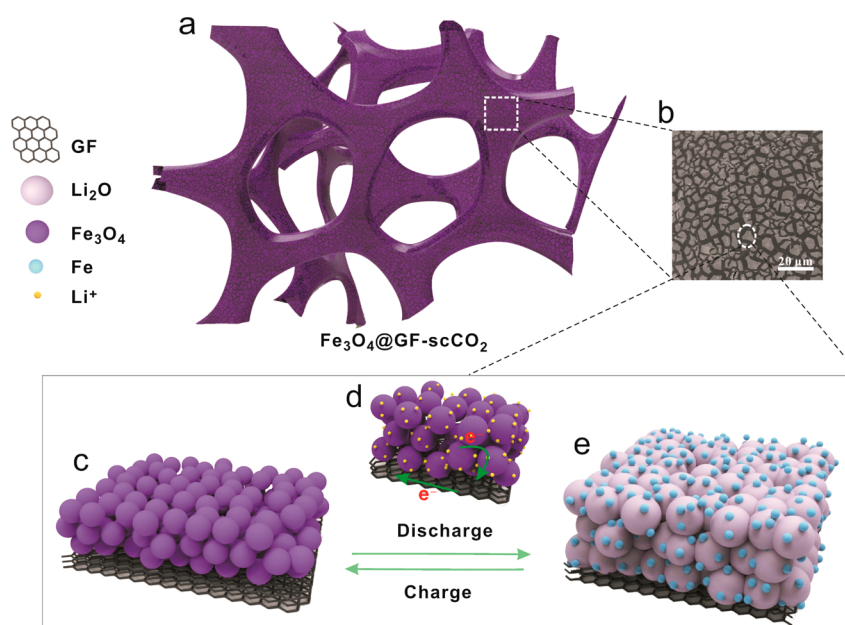
Figure 1. Scheme of the discharge and charge behavior for the Fe_3O_4@GF−$scCO_2$. (a) Schematic illustration of the 3D structure of Fe_3O_4@GF−$scCO_2$. (b) Low-resolution SEM image of the typical surface morphology of Fe_3O_4@GF−$scCO_2$. Schematic illustration of the typcial GF surface anchored Fe_3O_4 nanoparticles (c) after charge, (d) during electrochemical reaction, and (e) after discharge. The gray, purple, blue and yellow spheres correspond to the Li_2O, Fe_3O_4 NPs, Fe, and Li^+, respectively. The black hexagonal honeycomb structure corresponds to GF. The arrows indicate the transfer direction of the electrons.
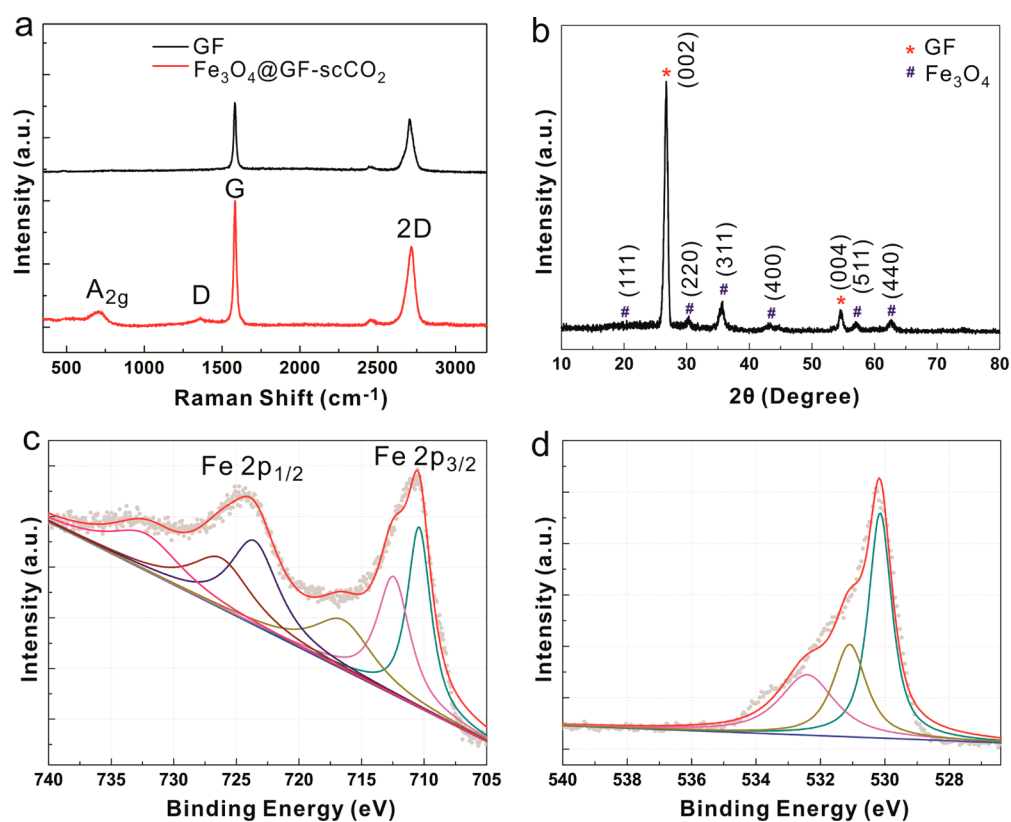

Figure 2. (a) Raman spectra of GF and Fe_3O_4@GF−$scCO_2$. (b) X-ray diffraction patterns of Fe_3O_4@GF−$scCO_2$. (c and d) X-ray photoelectron spectroscopy of Fe_3O_4@GF−$scCO_2$, in which (c) corresponds to the Fe 2p states and (d) corresponds to O 1s states.

dimensional graphene using atomic layer deposited (ALD) ZnO sacrificial layer assisted hydrolysis and demonstrated a long cycle life with a fast discharge−charge capability due to strong adherence of the active material.[25] However, the complex synthesis procedures (such as oxygen plasma treatment and ALD) with the obvious consequent graphene damage do not facilitate its general use in commercially viable applications.

Despite the above-mentioned progress, developing more effective methods to tightly bound self-organized, small size distribution Fe_3O_4 NPs layers to graphene frameworks remains both crucial and challenging. Supercritical carbon dioxide ($scCO_2$) is an effective strategy for synthesizing superior ultrafine and uniform nanomaterials due to its unique features of low viscosity, zero surface tension, and high diffusivity.[26] Moreover, the relatively low temperature and the stability of CO_2 allows most compounds to be synthesized with negligible damage.[27] Here, we present a new approach which makes use of $scCO_2$ to efficiently anchor Fe_3O_4 NPs on graphene foam (GF) in a single step. Without the use of any surfactants, we obtain moderately spaced Fe_3O_4 NP arrays on the surface of GF. The good contact established between Fe_3O_4 and GF not only can prevent the aggregation of Fe_3O_4 NPs but also can provide an efficient medium for lithium ion and electron transport. Our Fe_3O_4@GF−$scCO_2$ based electrodes demonstrate a high capacity of nearly 1200 mAh g^{-1} and a long cycle life up to five hundred cycles with a high-rate discharge−charge capability.

■ RESULTS AND DISCUSSION

As shown in Figure 1a, GF is composed with interconnected graphene sheets, which can serve as template for the deposition of Fe_3O_4 NPs. The CVD grown GF rather than the other carbon materials was chosen because of its excellent conductivity, large specific surface area and freestanding ability. The discontinuous Fe_3O_4 flakes with micrometer scale are constituted by homogeneously distributed Fe_3O_4 NPs, and are easily observed on the surface of GF (Figure 1a and Supporting Information, Figure S1a). There are numerous channels between the discontinuous Fe_3O_4 nanostructures (Figure 1b). Homogeneously distributed Fe_3O_4 NPs are anchored on GF tightly with the help of $scCO_2$ (Figure 1c and Supporting Information, Figure S1b,c). The partially covered and strong contact provides efficient transportation of electron between the Fe_3O_4 NPs and the GF, as well as ion transport between electrolyte and active materials (Figure 1d). Thus, the GF can be directly employed as a current collector without requiring the addition of any other binder or conducting agent. Moreover, the intact contact between Fe_3O_4 and GF prevents the aggregation of Fe_3O_4 particles and any electrical disconnection between the active material and the current collector caused by volume change (Supporting Information, Figure S1b,e).

The Raman spectra of GF and Fe_3O_4@GF−$scCO_2$ are presented in Figure 2a. The black curve shows two typical peaks of graphene, centered at 1580 and 2720 cm^{-1} and corresponding to G band and 2D band, respectively. The absence of the disorder-induced D band at 1350 cm^{-1} indicates the high quality of the GF.[28] Also, the Raman intensity of the G band is higher than the 2D band, which is consistent with the multilayer property of graphene foam.[29] This makes it sufficiently rigid to serve as a scaffold for battery electrodes. After Fe_3O_4 NPs were anchored on GF, two additional peaks were observed. The stronger one centered at 667 cm^{-1} corresponds to the A_{1g} mode of Fe_3O_4.[19] The small D peak located at 1350 cm^{-1} ($I_D/I_G = 0.017$) indicates only very few defects are introduced to the GF by the anchoring of Fe_3O_4, confirming our approach is far less aggressive than other Fe_3O_4 deposition methods such as ozone plasma treatments and ALD deposition.[25] This makes it appropriate to serve as a high-conductivity framework to improve the electrical conductivity

of the whole electrode. The obtained Fe_3O_4@GF−$scCO_2$ was characterized by X-ray diffraction (XRD) (Figure 2b). The two typical diffraction peaks centered at 26.5° and 54.6° are attributed to the (002) and (004) reflections of graphitic carbon, respectively (JCPDS card 75−1621).[30] There are another six peaks appearing in the composites, which indicate the (111), (220), (311), (400), (511) and (440) reflections of Fe_3O_4 (JCPDS card 19−0629).[19] To further confirm the XRD results, we examined the oxidation states and composition of iron oxides by X-ray photoelectron spectroscopy (XPS). The wide survey XPS spectrum of Fe_3O_4@GF−$scCO_2$, as displayed in Figure S2 (Supporting Information), shows predominant signals of carbon, oxygen, and iron. The Fe 2p spectrum shows the presence of Fe^{3+} and Fe^{2+}, as seen in Figure 2c, we can assign the peak at around 710.4 eV to a $Fe^{III}_{3/2}$ configuration. The other smaller peak located at around 712.4 eV is attributed to a $Fe^{II}_{3/2}$ configuration.[31] The other spin−orbit component, the $2p_{1/2}$, appears at 723.6 and 725.2 eV which correspond to 3+ and 2+ states, respectively. The two weak peaks at 716.4 and 732.2 eV are the Fe^{2+} shakeup satellite peaks.[32] The O 1s spectra of the as-prepared samples is shown in Figure 2d. The peak centered at 530.1 eV corresponds to the oxygen in the Fe_3O_4 crystal lattice, while the peaks at about 531.2 and 532.4 eV correspond to chemisorbed oxygen caused by surface hydroxylationl.[33,34] By analyzing the results of Raman, XRD, and XPS, we can confirm the Fe_3O_4 particles, and no iron nitrate hydrate or other iron oxides are detected.

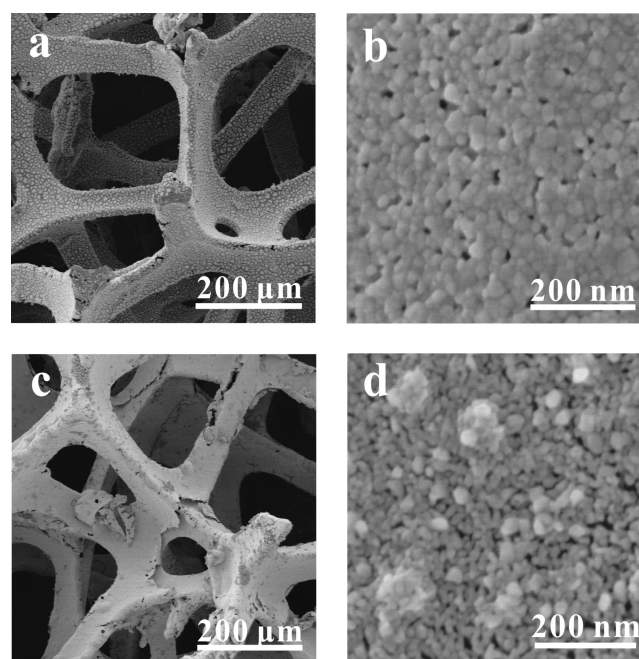Figure 3a shows the low-magnification image of Fe_3O_4@GF−$scCO_2$. It is obvious that homogeneous Fe_3O_4 NPs

Figure 3. Low-magnification SEM image of (a) Fe_3O_4@GF−$scCO_2$ and (c) Fe_3O_4@GF and representative enlarged morphology images of (b) Fe_3O_4@GF−$scCO_2$ and (d) Fe_3O_4@GF.

anchored on GF has some channels. The total area of the channels occupies about 40% of the whole surface (Supporting Information, Figure S3b). Figure 3b shows a high-magnification image of Fe_3O_4@GF−$scCO_2$ that clearly demonstrates that the diameter of the Fe_3O_4 NPs has a narrow distribution. Between the NPs, there are evenly distributed nanopores, which take up
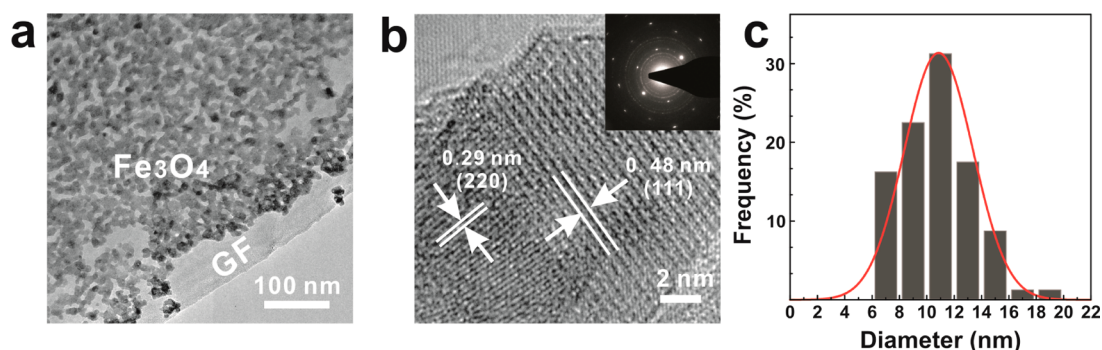
Figure 4. TEM images of (a) GF and Fe_3O_4 NPs. (b) HRTEM of an individual Fe_3O_4; (inset) SAED patterns of Fe_3O_4@GF−scCO$_2$. (c) The size distribution of Fe_3O_4 NPs in Fe_3O_4@GF−scCO$_2$.
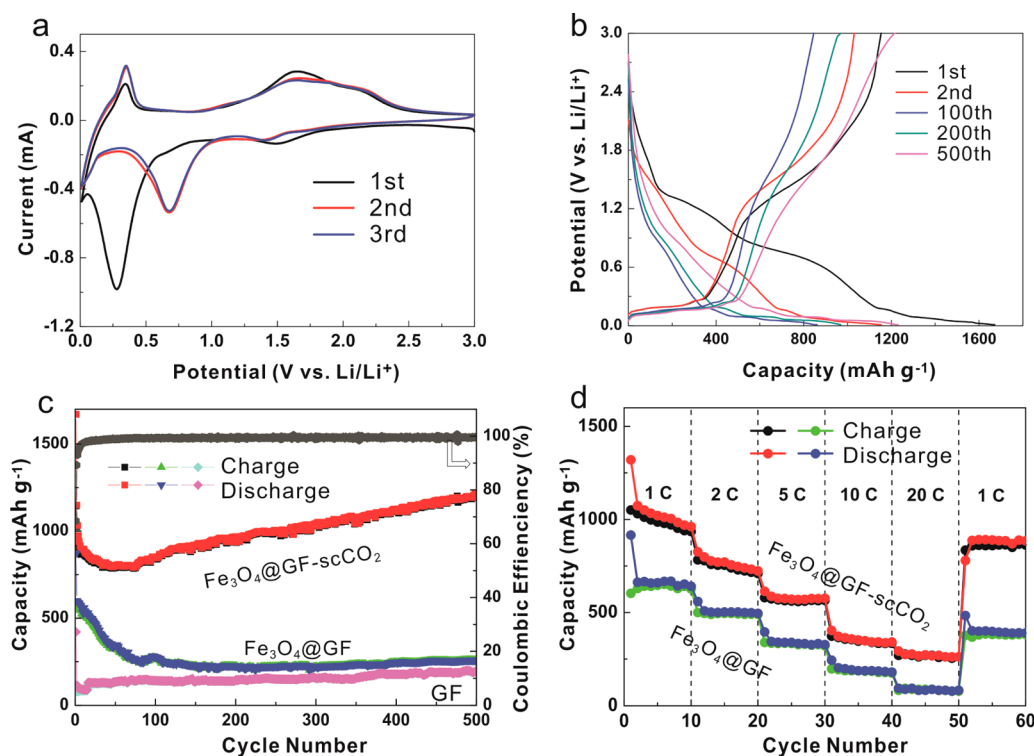

Figure 5. (a) CV curves of Fe_3O_4@GF−scCO$_2$ electrode at a sweeping rate of 1 mV s^{-1} in a range of 0.01−3.0 V. (b) The 1st, 2nd, 100th, 200th, and 500th discharge−charge voltage−capacity curves of Fe_3O_4@GF−scCO$_2$ electrode. (c) Cycling performance of GF, Fe_3O_4@GF, and Fe_3O_4@ GF−scCO$_2$ at 1C (924 mA g^{-1}) rate. (d) Rate performance of Fe_3O_4@GF−scCO$_2$ electrode and Fe_3O_4@GF electrode.

8.3% of the area, as shown in Figure 3b and Supporting Information, Figure S1c. The channels and nanopores in the structure can enhance lithium-ion diffusion, ensure a high electrode−electrolyte contact area, and provide the means to accommodate volume expansion (Supporting Information, Figures S1c,f and S3c,d), and thus improve cycling performance. To validate the pivotal effect of a scCO$_2$ medium, we performed a controlled experiment for comparison. GF was soaked in iron nitrate ethanol solution under the same conditions but without scCO$_2$. Figure 3c reveals the GF skeleton was loosely coated by a Fe_3O_4 layer without any obvious channels or pores, which should lead to serious volume expansion problems and, hence, capacity degradation during cycling. The particle size of Fe_3O_4 is random and aggregates a lot as shown in Figure 3d.

Figure 4a shows a representative transmission electron microscopic (TEM) evaluation of the GF and Fe_3O_4 NPs. Fe_3O_4 NPs with average size of 11 ± 4 nm were uniformly

distributed and well adhered on graphene sheets in the Fe_3O_4@ GF−scCO$_2$ (Figure 4a,c). The void accommodates volume changes during cycling reactions. The HRTEM image of an individual Fe_3O_4 is shown in Figure 4b. The lattice fringes with *d*-spacing of 0.29 and 0.48 nm can be assigned to (220) and (111) planes of cubic Fe_3O_4. The electron diffraction pattern from a selected area shows the characteristics of both Fe_3O_4 and graphene, as shown in the inset of Figure 4b.

To determine the electrochemical performance of the Fe_3O_4@GF−scCO$_2$ electrodes, we assembled them into coin cells with lithium foils as reference electrodes. The lithium storage behavior was characterized by cyclic voltammetry. As shown in Figure 5a, in the first cycle, three well-defined reduction peaks can be observed at 1.51, 0.61, and 0.28 V. The peak located at 1.51 V corresponds to the structure transition caused by the insertion of lithium ions into Fe_3O_4 into Fe_3O_4 $(Fe_3O_4 + xLi^+ + xe^- \rightarrow Li_xFe_3O_4)$ and peaks centered at 0.61 V correspond to the further transformation of $Li_xFe_3O_4$ to Fe^0 by

22530

dx.doi.org/10.1021/am5066255 | ACS Appl. Mater. Interfaces 2014, 6, 22527−22533

a conversion reaction $[Li_xFe_3O_4 + (8−x)Li^+ + (8−x)e^− → 4Li_2O + 3Fe]$. In addition, the formation of amorphous Li_2O exacerbates the irreversible reaction with the electrolyte, which is consistent with previous works.[35] The peak centered at 0.28 V corresponds to the irreversible reactions and cannot be observed in the second and third cycles. The subsequent cycles show good reproducibility, in which the cathodic lithium insertion mainly occurs at 1.44 and 0.68 V, whereas the anodic lithium extraction occurs at 1.65 and 2.17 V due to a two-step reversible reaction, namely, from Fe^0 to Fe^{2+} and Fe^{2+} to Fe^{3+}.[36] Apart from the reaction peaks for Fe_3O_4, the curves also show another two redox peaks located at 0.12 and 0.32 V, which correspond to the lithiation and delithiation of GF, respectively.[37] The discharge−charge voltage−capacity curves of Fe_3O_4@GF−scCO_2 for the 1st, 2nd, 100th, 200th, and 500th cycles at 1C rate between 0.01 and 3.00 V and are illustrated in Figure 5b. It can be seen from Figure 5b that the composite delivers a high discharge capacity of 1671.4 mAh g$^{−1}$ and a reversible charge capacity of 1144.6 mAh g$^{−1}$ at the first cycle. The irreversible capacity loss can be attributed to the inevitable formation of solid electrolyte interphase (SEI), decomposition of the electrolyte, or both. In the first cycle, the discharge voltage plateaus at ∼0.28 V, which is different from other cycles. From this phenomenon, it can be confirmed that the irreversible reaction only occurs in the first cycle. One can also observe that the low-potential plateau broadens upon extended cycling (100−500th), whereas the high-potential almost disappears, which is well consistent with the documented results. This phenomenon might be indicative of a change in lithiation and delithiation reactions after deep cycles.[38] To elaborate the advantages of employing scCO$_2$ over cycling stability, we conducted controlled experiments to offer comparisons with the Fe_3O_4@GF electrode. Discharge−charge measurements were performed at 1C (924 mA g$^{−1}$) rate to 500 cycles in ambient conditions. As shown in Figure 5c, a pure GF electrode delivers a capacity of ∼200 mAh g$^{−1}$ after 500 cycles. The capacity of Fe_3O_4@GF−scCO_2 electrode decreases in the initial 100 cycles and then increases to ∼1200 mAh g$^{−1}$ after 500 cycles, whereas the capacity of Fe_3O_4@GF electrode drops off significantly to ∼210 mAh g$^{−1}$ in the initial 100 cycles and then rises up slightly to ∼260 mAh g$^{−1}$ at the subsequent cycles. The capacity of the Fe_3O_4@GF−scCO_2 electrode obviously demonstrates its excellent electrochemical performance over Fe_3O_4@GF. It is worth noting that the capacity of Fe_3O_4@GF−scCO_2 increases gradually, which continues up to 500 cycles. The continuous increment in capacity should be resulted from the pulverization of Fe_3O_4 NPs during repeated cycling (Supporting Information, Figure S4b), which increases the surface area of the electrode and release more active sites for lithium storage. In addition, the smaller grain size of the Fe_3O_4 NPs (8 ± 2 nm; Supporting Information, Figure S4) could improve the contact with the GF and would increase the overall conductivity of the electrodes (in accordance with the impedance result; Supporting Information, Figure S5, it also shows the superior conductivity of Fe_3O_4@GF−scCO_2 electrode over Fe_3O_4@GF electrode before and after 500 cycles). As a result, the charge transfer kinetics will also be significantly improved, resulting in the increment of the capacity in repeated cycles.[25] To test the rate performance of the Fe_3O_4@GF−scCO_2 electrode, we conducted galvanostatic discharge−charge measurements at different C rates. As illustrated in Figure 5d, the capacity as high as 900 mAh g$^{−1}$ can be measured when the C rate returns back from 20 C to 1C, indicating its high stability and excellent reversibility, which is much better than the Fe_3O_4@GF anode at such high C rates. Compared to previous reports, the performance of as-prepared Fe_3O_4@GF−scCO_2 electrode is superior in specific capacity, rate capability, and cycling stability (Supporting Information, Figure S6).

CONCLUSION

In summary, we have developed a scCO$_2$-assisted one-step strategy for anchoring Fe_3O_4 NPs on GF. Without using any surfactant, the nanoparticles with a narrow distribution (11 ± 4 nm in diameter) are uniformly distributed and closely attached to the GF. The designed nanostructure of the electrode shortens the transport path of lithium-ion, increases the electrode/electrolyte contact area, minimizes strain during lithiation and delithiation, and is able to buffer volume expansion during cycling. The reversible specific capacity of Fe_3O_4@GF−scCO_2 reached 1200 mAh g$^{−1}$, which tends to grow continuously over as-tested 500 cycles at 924 mA g$^{−1}$ (1 C), showing a much enhanced capacity and excellent high-rate capability (about 300 mAh g$^{−1}$ at 20 C). The significant improvement in LIB performance and simplicity of using scCO$_2$ will greatly facilitate future research and applications for various kinds of metal oxides.

EXPERIMENTAL SECTION

Synthesis of Graphene Foam (GF). Graphene foam was directly grown on nickel foam (1.65 mm thick, Alantum Advanced Technology Materials, China) under ambient pressure chemical vapor deposition, and the nickel foam was cut into small disks (R = 12 mm). The growth procedure was conducted in a horizontal quartz tube fixed inside a high-temperature furnace (HTF 55322C Lindberg/Blue M). The growth protocol consisted of four steps: (1) the nickel foam was heated to 1000 °C in 30 min under the atmosphere of Ar (500 sccm) and H$_2$ (50 sccm), then annealed at 1000 °C for 10 min without changing the gas flow; (2) a nominal amount of CH$_4$ (5 sccm) was brought into the reaction tube at ambient pressure for 5 min; (3) the samples were cooled to room temperature naturally with Ar (500 sccm); and (4) the nickel backbone was etched by HNO$_3$ solution (1 M) for 12 h. The GFs were then washed by ultrapure water and ethanol.

Fabrication of Fe_3O_4@GF−scCO_2. Iron(III) nitrate nonahydrate absolute ethanol solution (1.25 wt %, 10 mL) and GF (about 0.5 mg) were loaded into a high-pressure stainless vessel with a volume of 25 mL. Then, carbon dioxide was injected by a high-pressure pump to 9.0 MPa at 45 °C. The vessel was put in the oven at 120 °C for 9 h. After the vessel was cooled to room temperature, the carbon dioxide was ejected. The materials were washed by absolute ethanol at least 5 times. After drying, the composites were put in the furnace at 450 °C for 2 h with a gas flow of 100 sccm Ar in order to achieve better interconnection of each component. The controlled experiments were conducted at the same condition except for the injection of the high-pressure CO$_2$.

Characterization. Raman spectroscopy was performed with a laser micro-Raman spectrometer (Renishaw in Via, Renishaw, 532 nm excitation wavelength). Scanning electron microscopy (SEM) images were obtained by Hitachi-S4800. The XPS measurements were conducted with Thermo Scientific, ESCALAB 250Xi. The measuring spot size was 500 μm, and the binding energies were calibrated by referencing the C 1s peak (284.8 eV). X-ray diffraction (XRD) measurement was performed with LabX XRD-6000 using Cu−Kα radiation over the range of 2θ = 10−80°. Thermogravimetric analysis (TGA) was conducted on a TGA Q600 (Thermal Analysis Instrument, Burlington) in air with a heating rate of 10 °C/min from room temperature to 800 °C. All of the specific capacities were calculated on the basis of the weight of Fe_3O_4 (Supporting

Information, Figure S7), and the mass of the entire electrode and Fe_3O_4 are shown in Table S1 (Supporting Information).

Electrochemical Measurements. Electrochemical measurements were conducted in standard CR2016 cell. The cells were assembled in an Ar-filled glovebox by directly using the as-prepared Fe_3O_4@GF–$scCO_2$ as working electrode without adding any binder or conductive agents and lithium metal circular foil (1.5 mm thick) as counter electrode. For comparison, the electrolyte used was a 1.0 M $LiPF_6$ solution in a mixture of ethylene carbonate (EC) and diethyl carbonate (DEC; 1:1 by volume). Galvanostatical charge–discharge tests were conducted at various current densities at the voltage range from 0.01 to 3.00 V with a multichannel battery tester (LAND CT 2001A, Wuhan LAND Electronics Co., Ltd.). The cyclic voltammetry (CV) tests were measured using electrochemical workstation (CHI610E, Chenhua, Shanghai) at a sweeping rate of 1 mV s^{-1} with the voltage ranging from 0.01 to 3.00 V. Electrochemical impedance spectroscopy (EIS) were measured in the frequency range from 100 kHz to 0.01 Hz on a electrochemical workstation (Im6e, Zahner).

■ ASSOCIATED CONTENT

Ⓢ Supporting Information

SEM images of Fe_3O_4@GF–$scCO_2$ before and after 500 cycles, TEM image and size distribution of Fe_3O_4@GF–$scCO_2$ after 500 cycles, EIS data for synthesized electrodes before and after 500 cycles, TGA of Fe_3O_4@GF–$scCO_2$, and the comparison of the recent studies on Fe_3O_4@graphene composites. This material is available free of charge via the Internet at http://pubs.acs.org.

■ AUTHOR INFORMATION

Corresponding Author
*Tel: (+)86-027-6875-5867. Fax: (+)86-027-6875-5867. E-mail: leifu@whu.edu.cn.

Author Contributions
L.F. developed the concept and conceived the experiments. X.B.H. carried out the experiments. L.F. and X.B.H. wrote the manuscript. L.F., X.B.H., M.H.M., M.Q.Z; Y.Y.S., L.F.C., Y.H.X., T.Z., X.P.A., and M.H.R. contributed to data analysis and scientific discussion.

Notes
The authors declare no competing financial interest.

■ ACKNOWLEDGMENTS

■ REFERENCES

(1) Armand, M.; Tarascon, J. M. Building Better Batteries. *Nature* **2008**, *451*, 652–657.

(2) Goodenough, J. B.; Kim, Y. Challenges for Rechargeable Li Batteries. *Chem. Mater.* **2010**, *22*, 587–603.

(3) Kang, B.; Ceder, G. Battery Materials for Ultrafast Charging and Discharging. *Nature* **2009**, *458*, 190–193.

(4) Mitra, S.; Poizot, P.; Finke, A.; Tarascon, J. M. Growth and Electrochemical Characterization versus Lithium of Fe_3O_4 Electrodes Made via Electrodeposition. *Adv. Funct. Mater.* **2006**, *16*, 2281–2287.

(5) Poizot, P.; Lauruelle, S.; Grugeon, S.; Dupont, L.; Tarascon, J. M. Nano-Sized Transition-Metal Oxides as Negative-Electrode Materials for Lithium-Ion Batteries. *Nature* **2000**, *407*, 496–499.

(6) Zhang, W. M.; Wu, X. L.; Hu, J. S.; Guo, Y. G.; Wan, L. J. Carbon Coated Fe_3O_4 Nanospindles as a Superior Anode Material for Lithium-Ion Batteries. *Adv. Funct. Mater.* **2008**, *18*, 3941–3946.

(7) Wu, Z. S.; Ren, W. C.; Wen, L.; Gao, L. B.; Zhao, J. P.; Chen, Z. P.; Zhou, G. M.; Li, F.; Cheng, H. M. Graphene Anchored with Co_3O_4 Nanoparticles as Anode of Lithium Ion Batteries with Enhanced Reversible Capacity and Cyclic Performance. *ACS Nano* **2010**, *4*, 3187–3194.

(8) Ji, L. W.; Tan, Z. K.; Kuykendall, T. R.; Aloni, S.; Xun, S. D.; Lin, E.; Battaglia, V.; Zhang, Y. G. Fe_3O_4 Nanoparticle-Integrated Graphene Sheets for High-Performance Half and Full Lithium Ion Cells. *Phys. Chem. Chem. Phys.* **2011**, *13*, 7170–7177.

(9) Taberna, P. L.; Mitra, S.; Poizot, P.; Simon, P.; Tarascon, J. M. High Rate Capabilities Fe_3O_4-Based Cu Nano-Architectured Electrodes for Lithium-Ion Battery Applications. *Nat. Mater.* **2006**, *5*, 567–573.

(10) Chen, J.; Xu, L. N.; Li, W. Y.; Gou, X. L. α-Fe_2O_3 Nanotubes in Gas Sensor and Lithium-Ion Battery Applications. *Adv. Mater.* **2005**, *17*, 582–586.

(11) Zhu, S. L.; Marschilok, A. C.; Takeuchi, E. S.; Yee, G. T.; Wang, G. B.; Takeuchia, K. J. Nanocrystalline Magnetite: Synthetic Crystallite Size Control and Resulting Magnetic and Electrochemical Properties. *J. Electrochem. Soc.* **2010**, *157*, A1158–A1163.

(12) Koo, B.; Xiong, H.; Slater, M. D.; Prakapenka, V. B.; Balasubramanian, M.; Podsiadlo, P.; Johnson, C. S.; Rajh, T.; Shevchenko, E. V. Hollow Iron Oxide Nanoparticles for Application in Lithium Ion Batteries. *Nano Lett.* **2012**, *12*, 2429–2435.

(13) Liu, J. P.; Li, Y. Y.; Fan, H. J.; Zhu, Z. H.; Jiang, J.; Ding, R. M.; Hu, Y. Y.; Huang, X. T. Iron Oxide-Based Nanotube Arrays Derived from Sacrificial Template-Accelerated Hydrolysis: Large-Area Design and Reversible Lithium Storage. *Chem. Mater.* **2010**, *22*, 212–217.

(14) Zhou, G. M.; Wang, D. W.; Li, F.; Zhang, L. L.; Li, N.; Wu, Z. S.; Wen, L.; Lu, G. Q.; Cheng, H. M. Graphene-Wrapped Fe_3O_4 Anode Material with Improved Reversible Capacity and Cyclic Stability for Lithium Ion Batteries. *Chem. Mater.* **2010**, *22*, 5306–5313.

(15) Wu, Y.; Wei, Y.; Wang, J. P.; Jiang, K. L.; Fan, S. S. Conformal Fe_3O_4 Sheath on Aligned Carbon Nanotube Scaffolds as High-Performance Anodes for Lithium Ion Batteries. *Nano Lett.* **2013**, *13*, 818–823.

(16) Ban, C. M.; Wu, Z. C.; Gillaspie, D. T.; Chen, L.; Yan, Y. F.; Blackburn, J. L.; Dillon, A. C. Nanostructured Fe_3O_4/SWNT Electrode: Binder-Free and High-Rate Li-Ion Anode. *Adv. Mater.* **2010**, *22*, E145–E149.

(17) Zhu, J. X.; Yin, Z. Y.; Yang, D.; Sun, T.; Yu, H.; Hoster, H. E.; Hng, H. H.; Zhang, H.; Yan, Q. Y. Hierarchical Hollow Spheres Composed of Ultrathin Fe_2O_3 Nanosheets for Lithium Storage and Photocatalytic Water Oxidation. *Energy Environ. Sci.* **2013**, *6*, 987–993.

(18) Hou, J. B.; Shao, Y. Y.; Ellis, M. W.; Moore, R. B.; Yi, B. L. Graphene-Based Electrochemical Energy Conversion and Storage: Fuel Cells, Supercapacitors and Lithium Ion Batteries. *Phys. Chem. Chem. Phys.* **2011**, *13*, 15384–15402.

(19) Li, N.; Chen, Z. P.; Ren, W. C.; Li, F.; Cheng, H. M. Flexible Graphene-Based Lithium Ion Batteries with Ultrafast Charge and Discharge Rates. *Proc. Natl. Acad. Sci. U.S.A.* **2012**, *109*, 17360–17365.

(20) Cao, X. H.; Zheng, B.; Rui, X. H.; Shi, W. H.; Yan, Q. Y.; Zhang, H. Metal Oxide-Coated Three-Dimensional Graphene Prepared by the Use of Metal–Organic Frameworks as Precursors. *Angew. Chem., Int. Ed.* **2014**, *53*, 1404–1409.

(21) Bhuvaneswari, S.; Pratheeksha, P. M.; Anandan, S.; Rangappa, D.; Gopalanb, R.; Raoa, T. N. Efficient Reduced Graphene Oxide Grafted Porous Fe_3O_4 Composite as a High Performance Anode Material for Li-Ion Batteries. *Phys. Chem. Chem. Phys.* **2014**, *16*, 5284–5294.

(22) Cai, M. C.; Qian, H.; Wei, Z. K.; Chen, J. J.; Zheng, M. S.; Dong, Q. F. Polyvinyl Pyrrolidone-Assisted Synthesis of a Fe_3O_4/ Graphene Composite with Excellent Lithium Storage Properties. *RSC Adv.* **2014**, *4*, 6379–6382.

(23) Zhuo, L. H.; Wu, Y. Q.; Wang, L. Y.; Ming, J.; Yu, Y. C.; Zhang, X. B.; Zhao, F. Y. CO_2-Expanded Ethanol Chemical Synthesis of a

Fe$_3$O$_4$@Graphene Composite and its Good Electrochemical Properties as Anode Material for Li-Ion Batteries. *J. Mater. Chem. A* **2013**, *1*, 3954−3960.

(24) Wei, W.; Yang, S. B.; Zhou, H. X.; Lieberwirth, I.; Feng, X. L.; Müllen, K. 3D Graphene Foams Cross-linked with Pre-Encapsulated Fe$_3$O$_4$ Nanospheres for Enhanced Lithium Storage. *Adv. Mater.* **2013**, *25*, 2909−2914.

(25) Luo, J. S.; Liu, J. L.; Zeng, Z. Y.; Ng, C. F.; Ma, L. J.; Zhang, H.; Lin, J. Y.; Shen, Z. X.; Fan, H. J. Three-Dimensional Graphene Foam Supported Fe$_3$O$_4$ Lithium Battery Anodes with Long Cycle Life and High Rate Capability. *Nano Lett.* **2013**, *13*, 6136−6143.

(26) Seki, T.; Grunwaldt, J. D.; Baiker, A. Heterogeneous Catalytic Hydrogenation in Supercritical Fluids: Potential and Limitations. *Ind. Eng. Chem. Res.* **2008**, *47*, 4561−4585.

(27) DeSimone, J. M.; Tumas, W. *Green Chemistry Using Liquid and Supercritical Carbon Dioxide*; Oxford University Press: New York, 2003.

(28) Malard, L. M.; Pimenta, M. A.; Dresselhaus, G.; Dresselhaus, M. S. Raman Spectroscopy in Graphene. *Phys. Rep.* **2009**, *473*, 51−87.

(29) Chen, Z. P.; Ren, W. C.; Gao, L. B.; Liu, B. L.; Pei, S. F.; Cheng, H. M. Three-Dimensional Flexible and Conductive Interconnected Graphene Networks Grown by Chemical Vapour Deposition. *Nat. Mater.* **2011**, *10*, 424−428.

(30) Dong, X. C.; Xu, H.; Wang, X. W.; Huang, Y. X.; Chan-Park, M. B.; Zhang, H.; Wang, L. H.; Huang, W.; Chen, P. 3D Graphene-Cobalt Oxide Electrode for High-Performance Supercapacitor and Enzymeless Glucose Detection. *ACS Nano* **2012**, *6*, 3206−3213.

(31) Li, P.; Jiang, E. Y.; Bai, H. L. Fabrication of Ultrathin Epitaxial γ-Fe$_2$O$_3$ Films by Reactive Sputtering. *J. Phys. D: Appl. Phys.* **2011**, *44*, 075003.

(32) Fujii, T.; de Groot, F. M. F.; Sawatzky, G. A.; Voogt, F. C.; Hibma, T.; Okada, K. In Situ XPS Analysis of Various Iron Oxide Films Grown by NO$_2$-Assisted Molecular-Beam Epitaxy. *Phys. Rev. B* **1999**, *59*, 3195−3202.

(33) Yamashita, T.; Hayes, P. Analysis of XPS Spectra of Fe^{2+} and Fe^{3+} Ions in Oxide Materials. *Appl. Surf. Sci.* **2008**, *254*, 2441−2449.

(34) Bhargava, G.; Gouzman, I.; Chun, C. M.; Ramanarayanan, T. A.; Bernasek, S. L. Characterization of the "Native" Surface Thin Film on Pure Polycrystalline Iron: A High-Resolution XPS and TEM Study. *Appl. Surf. Sci.* **2007**, *253*, 4322−4329.

(35) Xiao, Z.; Xia, Y.; Ren, Z.; Liu, Z.; Xu, G.; Chao, C.; Li, X.; Shen, G.; Han, G. R. Facile Synthesis of Single-Crystalline Mesoporous α-Fe$_2$O$_3$ and Fe$_3$O$_4$ Nanorods as Anode Materials for Lithium-Ion Batteries. *J. Mater. Chem.* **2012**, *22*, 20566−20573.

(36) Morales, J.; Sanchez, L.; Martin, F.; Berry, F.; Ren, X. L. Synthesis and Characterization of Nanometric Iron and Iron-Titanium Oxides by Mechanical Milling: Electrochemical Properties as Anodic Materials in Lithium Cells. *J. Electrochem. Soc.* **2005**, *152*, A1748−A1754.

(37) Frackowiak, E.; Béguin, F. Electrochemical Storage of Energy in Carbon Nanotubes and Nanostructured Carbons. *Carbon* **2002**, *40*, 1775−1787.

(38) He, C. N.; Wu, S.; Zhao, N. Q.; Shi, C. S.; Liu, E. Z.; Li, J. J. Carbon-Encapsulated Fe$_3$O$_4$ Nanoparticles as a High-Rate Lithium Ion Battery Anode Material. *ACS Nano* **2013**, *7*, 4459−4469.

22533

dx.doi.org/10.1021/am5066255 | *ACS Appl. Mater. Interfaces* 2014, 6, 22527−22533